High-frequency traveling-wave phononic cavity with sub-micron wavelength

Xin-Biao Xu,[1,4] Jia-Qi Wang,[1,4] Yuan-Hao Yang,[1,4] Weiting Wang,[2] Yan-Lei Zhang,[1,4] Bao-Zhen
Wang,[3] Chun-Hua Dong,[1,4] Luyan Sun,[2] Guang-Can Guo,[1,4] and Chang-Ling Zou[1,4,5,*]

[1]*CAS Key Laboratory of Quantum Information, University of Science and Technology of China, Hefei, Anhui 230026, China.*
[2]*Center for Quantum Information, Institute for Interdisciplinary*
Information Sciences, Tsinghua University, Beijing 100084, China
[3]*School of Civil Engineering, Hefei University of Technology, Hefei 230009, P.R. China.*
[4]*CAS Center For Excellence in Quantum Information and Quantum Physics,*
University of Science and Technology of China, Hefei, Anhui 230026, China
[5]*National Laboratory of Solid State Microstructures, Nanjing University, Nanjing 210093, China.*

Thin-film gallium nitride (GaN) as a proven piezoelectric material is a promising platform for the phononic integrated circuits, which hold great potential for scalable information processing processors. Here, an unsuspended traveling phononic resonator based on high-acoustic-index-contrast mechanism is realized in GaN-on-Sapphire with a frequency up to 5 GHz, which matches the typical superconducting qubit frequency. A fivefold increment in quality factor was found when temperature decreases from room temperature ($Q = 5000$) to 7 K ($Q = 30000$) and thus a frequency-quality factor product of 1.5×10^{14} is obtained. Higher quality factors are available when the fabrication process is further optimized. Our system shows great potential in hybrid quantum devices via circuit quantum acoustodynamics.

I. INTRODUCTION

Phonons have been widely used in sensing [1, 2] and classical communications [3]. For quantum information processing, phonons have also received significant attention because of their particular advantages compared to photons: phononic devices are widely accepted as a universal quantum transducer to connect various quantum systems such as, spin electrons [4, 5], quantum dots [6, 7], NV center [8, 9] and superconducting qubits [10–13]. Besides, phonons show ultralong lifetime compared to photons. The lifetime of a phononic mode up to 1.5 seconds has been demonstrated recently by carefully engineering the energy damping of the integrated phononic resonator, which makes phononic devices a good candidate for quantum memory [14]. As the propagation speed of phonons is five orders of magnitude smaller than that of microwave photons, the wavelength of the acoustic wave is also five orders of magnitude smaller than that of microwaves at the same frequency. By replacing the microwave devices in circuit quantum electrodynamics (QED) system with integrated phononic devices, the novel hybrid quantum systems show higher level of integration and scalability. Furthermore, the interaction between the superconducting artificial atoms and the GHz phonons, which is the so-called circuit quantum acoustodynamics (QAD), can explore novel and diverse dynamic processing [15–18]. Although different mechanical systems, such as suspended mechanical beams [19], bulk acoustic wave resonators [11] and phononic-crystal-based acoustic wave resonators [13] have been proposed and extensively studied for quantum information processing in the hybrid quantum systems, most of the phononic modes are localized or traveling without lateral confinement in the 2D phononic film [10, 12, 20].

Different from the above mechanical systems, an integrated and unsuspended phononic integrated circuit (PnIC) platform with traveling phonons has been recently proposed [21–24]. Similar to the optical waveguide, high-acoustic-index-contrast between the core waveguide and the substrate material allows the phonon waveguide to support discrete and confined phononic modes. The wavelength of the phonon waveguide ensures a small mode volume, which is essential to realize the strong coupling with other systems. Taking advantage of advanced nano-fabrication technologies, PnIC with different functional phononic devices can be constructed. Among them, high frequency integrated microresonator with high quality factor (Q) is one of the important devices [25, 26] as it promises large Q/V, which indicates a stronger phonon-matter interaction. Besides, higher frequency phononic modes also exhibit fewer thermal phonons at millikelvin temperatures that is critical for quantum coherence maintenance.

As a mature material, gallium nitride (GaN) shows good piezoelectric properties and great potential in PnIC [27]. In this work, a traveling phononic microring resonator with frequencies up to 5 GHz with submicro acoustic wavelength is demonstrated on the GaN-on-sapphire (GNOS) platform [21]. The mechanical Q-factor of the cavity increases from 5000 to 30000 when the temperature decreases from room temperature to 7 K.

As shown in Fig. 1(a), we focus on a simple PnIC configuration because it consists of all the essential passive ingredients for PnIC, including the efficient energy transduction, multiport couplers, and low-loss phonon guiding and confinement. The phononic mode in the microresonator is excited by the input fan-shaped interdigital transducer (IDT) as Fig. 1(d) shows, which converts the RF signal to the vibration of the phonon waveguide by
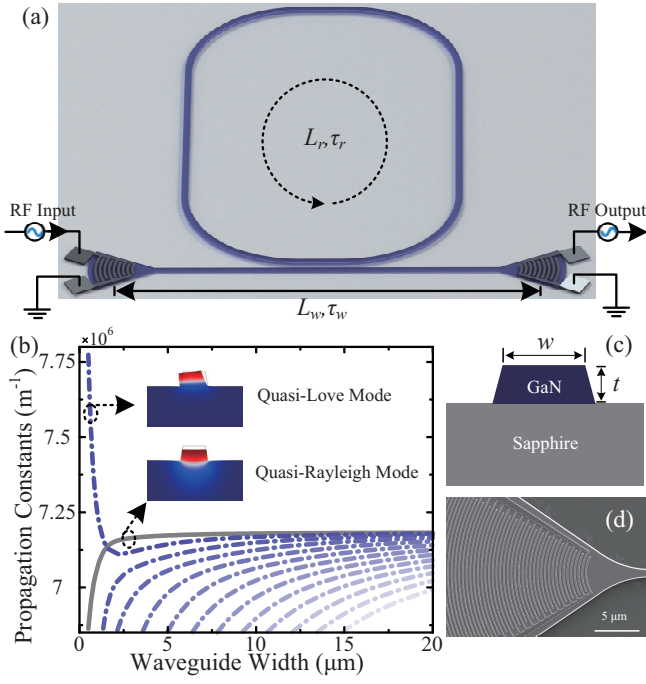
FIG. 1. (a) Schematic diagram of the integrated traveling wave phononic cavity. L_r and L_w are the total lengths of the racetrack resonator and the distance between two IDTs, respectively. τ_r and τ_w are the corresponding traveling times of phonon in cavity and waveguide with $\tau = L/v_g$, where v_g is the group velocity of the phonon. (b) The propagation constant of different phononic modes along [$1\bar{1}00$] direction versus the waveguide width when the phonon frequency is 5 GHz. The gray solid line represents the quasi-Rayleigh mode. The inset shows both the quasi-Love and Rayleigh modes. (c) The cross-section of the GaN waveguide on sapphire. (d) The SEM image of IDT structure.

the piezoelectric effect [21]. The inverse process occurs at the output IDT, where the energy of the phonon is converted to the output RF signal. The coupling between the bus waveguide and the cavity relies on the evanescent coupling. To match the frequencies of superconducting transmon qubits as well as the wavelength of optical photons for future phonon-based hybridized quantum circuits, we target at the working frequency of 5 GHz. Unlike the previously demonstrated unsuspended phononic circuit at lower frequencies, i.e. about 200 MHz in Ref. [21] and 3.5 GHz in Ref. [23], our devices require the structure dimension to be less than $1\,\mu m$ with the waveguide width of $w = 500$ nm and the corresponding acoustic wavelength is 916 nm. To enable the evanescent-field coupling between waveguides, we choose a thickness of the GaN film as $t = 320$ nm.

Properties of the phononic waveguide on the GaN-on-Sapphire system is numerically studied by the finite-element method (COMSOL Multiphysics). The displacement field distribution of the fundamental quasi-Love and quasi-Rayleigh modes are illustrated by the insets

of Fig. 1(b), with the corresponding cross-section of the waveguide being shown in Fig. 1(c). We choose the quasi-Rayleigh mode because it is dominated by the out-of-plane displacement and is more preferable for an efficient excitation by the IDT in GNOS. Also, the quasi-Rayleigh mode shows considerable evanescent field components in the substrate with a penetration depth of about 150 nm, implying efficient coupling between the waveguide and the ring resonator by setting a gap between them as $g = 300$ nm. In Fig. 1(b), the propagation constant of different phononic modes at 5 GHz along [$1\bar{1}00$] direction of sapphire as well as the direction of input waveguide is shown by varying the waveguide width w from 500 nm to $20\,\mu m$ corresponding to the waveguide width of the fan-shaped waveguide for IDT. It shows that the propagation constants of both quasi-Love and quasi-Rayleigh modes are insensitive to the width of the waveguide for $w > 2\,\mu m$, thus requiring a period of the IDT finger of 873 nm to match the propagation constant of the quasi-Rayleigh mode in the fan-shaped IDT region.

For the device fabrication, the phononic structures are patterned on the hydrogen silsesquioxane (HSQ, FOx-16) resist by an electron-beam lithography (EBL). The pattern is then transferred to the GaN film layer by an optimized full-etched inductively coupled plasma (ICP) dry etching processing. A second EBL is implemented to define the IDTs pattern using polymethyl methacrylate (PMMA) resist. 10-nm-thick titanium and 50-nm-thick aluminum are deposited followed by a subsequent lift-off process in acetone to realize the IDTs structure. Fig. 1(d) shows the device images of the IDT. The total length of the fabricated racetrack resonator is $L_r = 724\,\mu m$ with a bending radius $R = 50\,\mu m$. $\tau_r = L_r/v_{g,r}$ is the round-trip time, where $v_{g,r}$ is the average group velocity of the phonon traveling in the cavity. $L_w \approx 136\,\mu m$ and τ_w are the distance between two IDTs and the corresponding traveling time of phonons with $\tau_w = L_w/v_{g,w}$, where $v_{g,w}$ is group velocity of the phonon traveling in the waveguide.

The 5 GHz phononic circuit is characterized by measuring the transmission spectra of the system by a vector network analyzer (VNA) with the measurement setup shown in Fig. 1(a). The transmission spectra at room temperature and $T \approx 7$ K are plotted in Fig. 2. First of all, we could recognize an envelope of the spectrum modulation for the results at room temperature, as shown by the dashed pink line in Fig. 2(a). Such an envelope shows a limited IDT response frequency bandwidth in practice, and the bandwidth is inversely proportional to the number of IDT periods (21 for our devices) [28]. The extracted full width at half maximum and the center frequency of the IDT are about 150 MHz and 4.97 GHz, respectively, which matches well with the theoretical expectation of 160 MHz and 5 GHz. The modulation of the envelope resembles the sinusoidal interference fringes, with a period of about $\Lambda = 25.9$ MHz. There are two
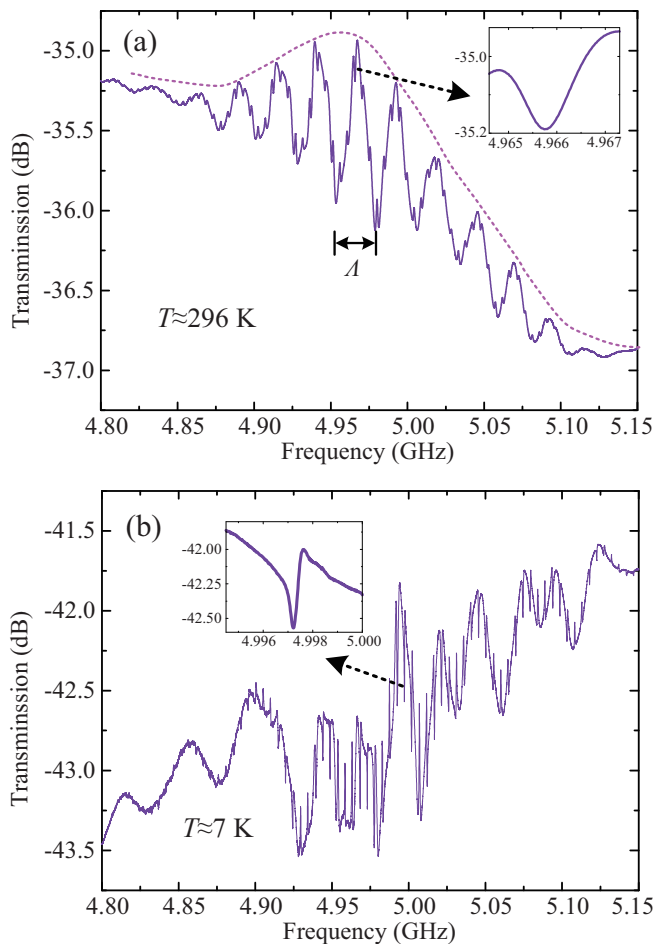
FIG. 2. (a) and (b) are the transmissions of the phonon cavity at room temperature (296 K) and low temperature (7 K), respectively. The insets are one of the enlarged resonances of the phononic cavity.

conjectures on the explanation of the interference: (1) the Mach-Zendel interferometer (MZI) mechanism with the interference between the direct phononic waveguide channel and the IDT cross-talk via air; (2) the phononic Fabry-Perot cavity effect in the straight waveguide due to the phonon reflections at two IDTs. For the two conjectures, the difference of the path lengths is L_w and $2L_w$, respectively. For the observed Λ, the two conjectures predict the group velocities of the phononic waveguide as $v_{g,w} = L_w \cdot \Lambda \approx 3522.4\,\mathrm{m/s}$ and $v_{g,w} = 2L_w \cdot \Lambda \approx 7044.8\,\mathrm{m/s}$, respectively.

For the resonator modes that we are interested in, we find many shallow dips or peaks on top of the background envelope. The inset shows the magnified spectrum of one selected dip, as indicated by the dashed arrow, corresponding to a Q-factor of a few thousands. For these shallow and sharp resonances, we can roughly estimate the FSR of the phononic racetrack cavity as $\mathrm{FSR}/2\pi = 4.8\,\mathrm{MHz}$, corresponding to a group velocity of the acoustic wave in the cavity as $\bar{v}_{g,r} = 3476\,\mathrm{m/s}$.

Comparing the group velocity to the results of $v_{g,w}$, we confirm that the modulation envelope of the spectrum with a period of Λ is attributed to the MZI mechanism.

The propagation loss of the phonon waveguide is determined by the geometry of the waveguide, the phononic properties of the material, and the nano-fabrication processes. Among those, the phononic properties of the material intrinsically limit the Q-factor of the cavity, which can be improved by upgrading the material growth technologies. Additionally, the intrinsic phonon loss of the material can also be reduced at lower temperatures [21, 23], and thus a higher Q-factor is expected. In Fig. 2(b), the transmission of the same device is measured at $T \approx 7\,\mathrm{K}$. It shows that the extinction ratio of the measured resonances is improved with the bandwidth decreasing obviously, implying a significant improvement of the Q-factor. The inset presents an enlarged resonance, which shows a Fano-type resonance [29] and is attributed to the interference between the phononic narrow resonances and the broadband modulation due to the MZI mechanism.

To eliminate the unwanted crosstalk and get an accurate Q-factor of the phonon cavity, a post-processing of the spectrum is implemented. By inverse Fourier transformation, the frequency-domain transmission of the system at $0-8\,\mathrm{GHz}$ is converted to the time-domain impulse response signal of the system, as shown by the blue lines in Fig. 3. We could imagine that when an impulse is excited and passes through the coupling region between the waveguide and the cavity, part of the pulse energy is coupled into the cavity. Each time the pulse in the cavity passes through the coupling region a small fraction of energy will couple out the cavity. So there are periodic pulses detected with a period of the round trip time τ_r of the phonon pulse in the phonon cavity, i.e. $\tau_r = L_r/v_{g,r}$, as the green pulses show in the inset in Fig. 3(a).

Besides, there are other two groups' signals with the same period as the yellow and purple pulses shown. These different groups of signals are due to the acoustic reflection by the IDTs, because the impulse will be bounced between the IDTs many times and sequentially excite the cavity modes each time when it passes through the ring cavity. The measured time delay $2\tau_w$ between the two adjacent groups is about $2\tau_w = 74\,\mathrm{ns}$, as is shown in Figs. 3(a) and (b), which exactly matches the time delay due to the pulse bouncing back and forth between the IDTs in the waveguide, i.e. $2/\Lambda = 77.2\,\mathrm{ns}$. Because the round trip time of the cavity τ_r is much longer than $2\tau_w$, there are several detected pulses from other groups in each round-trip time of the cavity as the inset of Fig. 3(a) shows. Similar temporal responses of the phononic cavity are tested for the results at $7\,\mathrm{K}$, as shown in Fig. 3(c) and (d). The time-delayed pulses are also observed, however, the background noise is larger compared to that at room temperature, especially during the $0-0.2\,\mu\mathrm{s}$. The noise may be attributed to the extra electronic noise for the
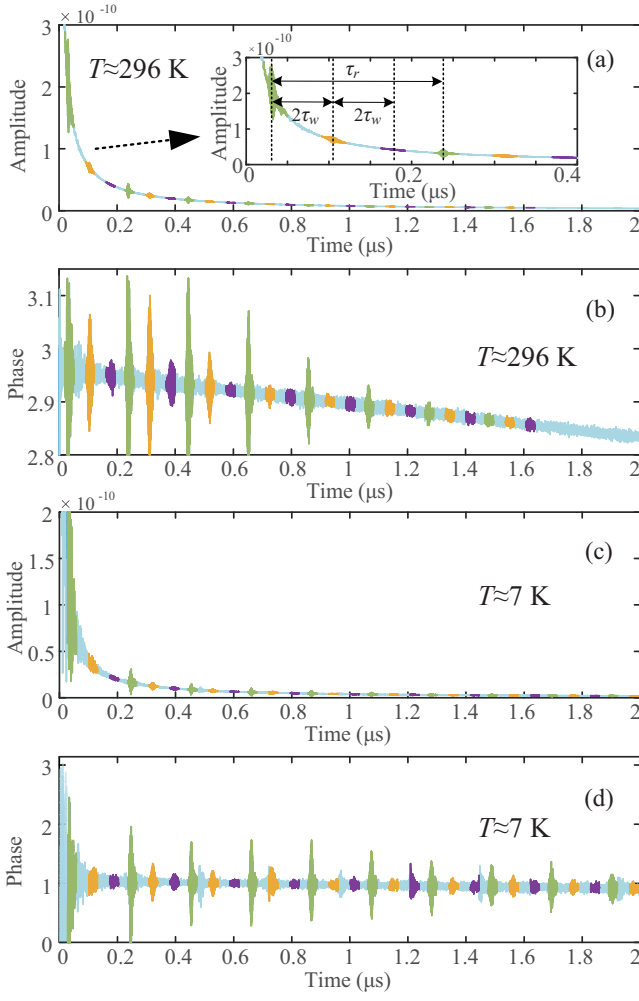
FIG. 4. (a) The energy decay rate of the phonon cavity at room temperature and $T \approx 7\,\mathrm{K}$. (b-c) The transmission of the cavity after the time domain filtering at room temperature and $T \approx 7\,\mathrm{K}$. As the first energy packet output from the cavity when $T \approx 7\,\mathrm{K}$ is neglected, the transmission shown in (c) are peaks. The insets show the fitting of the amplitude and phase of the resonance.

FIG. 3. (a-b) The amplitude and phase of the transmission in time domain at room temperature after a Fourier transform of the transmission spectra. The inset shows the enlarged graph of the curve with a time scale of $0 - 0.4\,\mu\mathrm{s}$. (c-d) The amplitude and phase of the transmission in time domain at $T \approx 7\,\mathrm{K}$.

measurements at the cryogenic temperatures.

To get a clean transmission spectrum of the system, we post-process the temporal response of the system by filtering out the green pulses, and thus the influences due to the reflections by IDTs are mitigated. First of all, the pulse energy is extracted and plotted in Fig. 4(a), where the blue and red circles are the results at $T \approx 7\,\mathrm{K}$ and room temperature, respectively. The evolutions of the pulse energy at these two temperatures are fitted by exponential decaying curves, giving the decay rates of $\kappa/2\pi = 1.37\,\mathrm{MHz}$ and $0.57\,\mathrm{MHz}$ with the corresponding loaded Q-factors of $Q = 3.65 \times 10^3$ and $Q = 8.772 \times 10^3$, respectively. Therefore, operating the phononic microring at the cryogenic temperature improves the lifetime by 2.4 times.

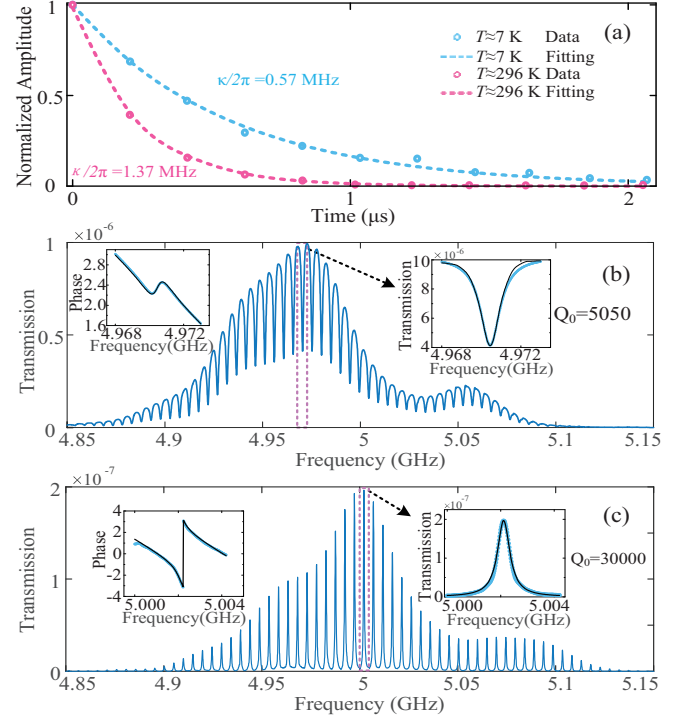The transmission spectra of the system are recon-

structed by converting the filtered time-domain signals back to the frequency-domain using Fourier transform, and the results are plotted in Figs. 4(b) and (c). Fig. 4(b) shows clean resonance spectrum with negligible background noise, and we could identify periodic resonance dips with $\mathrm{FSR}/2\pi = 4.8\,\mathrm{MHz}$. The insets show the typical results of the fitted resonance dip and the phase, giving a loaded quality factor $Q = 4.14 \times 10^3$ and intrinsic quality factor $Q_0 = 5.05 \times 10^3$. Similarly, the reconstructed spectrum at $T \approx 7\,\mathrm{K}$ [Fig. 4(c)] shows periodic spectral features without background noise. However, the resulted Lorentz peaks instead of dips are in sharp contrast to Fig.4(b). The reason is that when filtrating the impulses in Figs. 3(c) and (d), the first green pulse is neglected due to the significant noise background, and the remaining pulses correspond to the emission of the cavity instead of the transmission of the cavity. Therefore, the reconstructed spectrum is equivalent to a cavity emission spectrum received from the drop port of the cavity. By fitting the amplitude and phase of a resonance, as the insets show, we obtain the loaded and intrinsic quality factors $Q = 8.932 \times 10^3$ and $Q_0 = 3 \times 10^4$, respectively. Comparing the results at room temperature and $7\,\mathrm{K}$, the corresponding propagation losses of the phonon

waveguide are reduced from $\alpha \approx 4.343 \cdot \omega/(v_g \cdot Q_i) = 4.41\,\mathrm{dB\,mm^{-1}}$ to $1.29\,\mathrm{dB\,mm^{-1}}$. The intrinsic Q-factor has 5 times increment with the coupling between the cavity and the phonon waveguide changing from undercoupling to overcoupling as the phase curves shown in the insets of Figs. 4 (b) and (c). Besides, the peak of the IDT bandwidth has a blue-shift about $30\,\mathrm{MHz}$ due to the cooling down of the chip and a fQ product of 1.5×10^{14} is obtained at $T \approx 7\,\mathrm{K}$. It should be noted that both the loaded Q-factors obtained by fitting the resonance bandwidth are close to the values obtained by fitting the lifetime of the phonon in Fig. 4 (a), and both the amplitude and phase can be fitted well by the Lorentzian-type transmission of the micro-resonator. These results, therefore, justify the time-domain filtration operations in the data processing.

II.   CONCLUSION

In conclusion, a high frequency traveling wave phononic microring resonator based on the high-acoustic-index-contrast mechanism is demonstrated on GaN-on-Sapphire chip. The frequency of the phononic modes is up to the typical working frequency of superconducting qubits at about $5\,\mathrm{GHz}$. The phonon losses of the waveguide measured at room temperature and $T \approx 7\,\mathrm{K}$ are $\alpha \approx 4.41\,\mathrm{dB\,mm^{-1}}$ ($Q_0 = 5.05 \times 10^3$) and $1.29\,\mathrm{dB\,mm^{-1}}$ ($Q_0 = 3 \times 10^4$), respectively. A largest fQ product about 1.5×10^{14} is obtained finally. The phonon loss is expected to continue decreasing by further lowering the temperature and improving the nanofabrication technologies. We expect that such a phononic cavity can be employed to replace the superconducting microwave resonant cavity in the future for circuit quantum acoustodynamics. Besides, the phononic cavities system can be developed in the future for applications in topological phononics and acoustic filters. By applying electric fields in the system, phonon can be better controlled and modulated.

* clzou321@ustc.edu.cn

[1] K. Länge, B. E. Rapp, and M. Rapp, "Surface acoustic wave biosensors: a review," Anal. Bioanal. Chem. **391**, 1509 (2008).

[2] B. Liu, X. Chen, H. Cai, M. Mohammad Ali, X. Tian, L. Tao, Y. Yang, and T. Ren, "Surface acoustic wave devices for sensor applications," J. Semicond. **37**, 021001 (2016).

[3] C. Campbell, *Surface Acoustic Wave Devices for Mobile and Wireless Communications, Four-Volume Set* (Academic press, 1998).

[4] C. H. W. Barnes, J. M. Shilton, and A. M. Robinson, "Quantum computation using electrons trapped by surface acoustic waves," Phys. Rev. B **62**, 8410 (2000).

[5] S. Hermelin, S. Takada, M. Yamamoto, S. Tarucha, A. D. Wieck, L. Saminadayar, C. Bäuerle, and T. Meunier, "Electrons surfing on a sound wave as a platform for quantum optics with flying electrons," Nature **477**, 435 (2011).

[6] W. J. M. Naber, T. Fujisawa, H. W. Liu, and W. G. van der Wiel, "Surface-Acoustic-Wave-Induced Transport in a Double Quantum Dot," Phys. Rev. Lett. **96**, 136807 (2006).

[7] J. R. Gell, M. B. Ward, R. J. Young, R. M. Stevenson, P. Atkinson, D. Anderson, G. A. C. Jones, D. A. Ritchie, and A. J. Shields, "Modulation of single quantum dot energy levels by a surface-acoustic-wave," Appl. Phys. Lett. **93**, 081115 (2008).

[8] D. A. Golter, T. Oo, M. Amezcua, K. A. Stewart, and H. Wang, "Optomechanical Quantum Control of a Nitrogen-Vacancy Center in Diamond," Phys. Rev. Lett. **116**, 143602 (2016).

[9] D. A. Golter, T. Oo, M. Amezcua, I. Lekavicius, K. A. Stewart, and H. Wang, "Coupling a Surface Acoustic Wave to an Electron Spin in Diamond via a Dark State," Phys. Rev. X **6**, 041060 (2016).

[10] M. V. Gustafsson, T. Aref, A. F. Kockum, M. K. Ekstrom, G. Johansson, and P. Delsing, "Propagating phonons coupled to an artificial atom," Science **346**, 207 (2014).

[11] Y. Chu, P. Kharel, W. H. Renninger, L. D. Burkhart, L. Frunzio, P. T. Rakich, and R. J. Schoelkopf, "Quantum acoustics with superconducting qubits," Science **358**, 199 (2017).

[12] K. J. Satzinger, Y. P. Zhong, H.-S. Chang, G. A. Peairs, A. Bienfait, M.-H. Chou, A. Y. Cleland, C. R. Conner, É. Dumur, J. Grebel, I. Gutierrez, B. H. November, R. G. Povey, S. J. Whiteley, D. D. Awschalom, D. I. Schuster, and A. N. Cleland, "Quantum control of surface acoustic-wave phonons," Nature **563**, 661 (2018).

[13] M. Mirhosseini, A. Sipahigil, M. Kalaee, and O. Painter, "Superconducting qubit to optical photon transduction," Nature **588**, 599 (2020).

[14] G. S. MacCabe, H. Ren, J. Luo, J. D. Cohen, H. Zhou, A. Sipahigil, M. Mirhosseini, and O. Painter, "Nano-acoustic resonator with ultralong phonon lifetime," Science **370**, 840 (2020).

[15] A. Wallraff, D. I. Schuster, A. Blais, L. Frunzio, R.-S. Huang, J. Majer, S. Kumar, S. M. Girvin, and R. J. Schoelkopf, "Strong coupling of a single photon to a superconducting qubit using circuit quantum electrody-

namics," Nature **431**, 162 (2004).

[16] R. Manenti, A. F. Kockum, A. Patterson, T. Behrle, J. Rahamim, G. Tancredi, F. Nori, and P. J. Leek, "Circuit quantum acoustodynamics with surface acoustic waves," Nat. Commun. **8**, 975 (2017).

[17] L. Guo, A. Grimsmo, A. F. Kockum, M. Pletyukhov, and G. Johansson, "Giant acoustic atom: A single quantum system with a deterministic time delay," Phys. Rev. A **95**, 053821 (2017).

[18] G. Andersson, B. Suri, L. Guo, T. Aref, and P. Delsing, "Non-exponential decay of a giant artificial atom," Nat. Phys. **15**, 1123 (2019).

[19] M. D. Lahaye, J. Suh, P. M. Echternach, K. C. Schwab, and M. L. Roukes, "Nanomechanical measurements of a superconducting qubit," Nature **459**, 960 (2009).

[20] A. Bienfait, K. J. Satzinger, Y. P. Zhong, H.-S. Chang, M.-H. Chou, C. R. Conner, É. Dumur, J. Grebel, G. A. Peairs, R. G. Povey, and A. N. Cleland, "Phonon-mediated quantum state transfer and remote qubit entanglement," Science **364**, 368 (2019).

[21] W. Fu, Z. Shen, Y. Xu, C.-L. Zou, R. Cheng, X. Han, and H. X. Tang, "Phononic integrated circuitry and spin-orbit interaction of phonons," Nat. Commun. **10**, 2743 (2019).

[22] W. Wang, M. Shen, C.-L. Zou, W. Fu, Z. Shen, and H. X. Tang, "High-acoustic-index-contrast phononic circuits: Numerical modeling,"

[23] F. M. Mayor, W. Jiang, C. J. Sarabalis, T. P. McKenna, J. D. Witmer, and A. H. Safavi-Naeini, "Gigahertz Phononic Integrated Circuits on Thin-Film Lithium Niobate on Sapphire," Phys. Rev. Appl. **15**, 014039 (2021).

[24] L. Shao, D. Zhu, M. Colangelo, D. H. Lee, N. Sinclair, Y. Hu, P. T. Rakich, K. Lai, K. K. Berggren, and M. Loncar, "Electrical Control of Surface Acoustic Waves," arXiv:2101.01626 (2021).

[25] B. A. Moores, L. R. Sletten, J. J. Viennot, and K. W. Lehnert, "Cavity Quantum Acoustic Device in the Multimode Strong Coupling Regime," Phys. Rev. Lett. **120**, 227701 (2018).

[26] M. Shen, J. Xie, C.-L. Zou, Y. Xu, W. Fu, and H. X. Tang, "High frequency lithium niobate film-thickness-mode optomechanical resonator," Appl. Phys. Lett. **117**, 131104 (2020).

[27] M. Rais-Zadeh, V. J. Gokhale, A. Ansari, M. Faucher, D. Theron, Y. Cordier, and L. Buchaillot, "Gallium Nitride as an Electromechanical Material," J. Microelectromechanical Syst. **23**, 1252 (2014).

[28] W. Smith, H. Gerard, J. Collins, T. Reeder, and H. Shaw, "Design of Surface Wave Delay Lines with Interdigital Transducers," IEEE Trans. Microw. Theory Tech. **17**, 865 (1969).

[29] M. F. Limonov, M. V. Rybin, A. N. Poddubny, and Y. S. Kivshar, "Fano resonances in photonics," Nat. Photonics **11**, 543 (2017).